PHYSICAL REVIEW B **86**, 014404 (2012)

Topological and entanglement properties of resonating valence bond wave functions

Didier Poilblanc,[1] Norbert Schuch,[2,3] David Pérez-García,[4] and J. Ignacio Cirac[5]
[1]*Laboratoire de Physique Théorique, C.N.R.S. and Université de Toulouse, 31062 Toulouse, France*
[2]*Institute for Quantum Information, California Institute of Technology, MC 305-16, Pasadena, California 91125, USA*
[3]*Institut für Quanteninformation, RWTH Aachen, D-52056 Aachen, Germany*
[4]*Department of Mathematical Analysis, Faculty of Mathematics, UCM, Spain*
[5]*Max-Planck-Institut für Quantenoptik, Hans-Kopfermann-Str. 1, D-85748 Garching, Germany*
(Received 9 February 2012; published 6 July 2012)

We examine in details the connections between topological and entanglement properties of short-range resonating valence bond (RVB) wave functions using projected entangled pair states (PEPS) on kagome and square lattices on (quasi)infinite cylinders with generalized boundary conditions (and perimeters with up to 20 lattice spacings). By making use of disconnected topological sectors in the space of dimer lattice coverings, we explicitly derive (orthogonal) "minimally entangled" PEPS RVB states. For the kagome lattice, using the quantum Heisenberg antiferromagnet as a reference model, we obtain the finite-size scaling with increasing cylinder perimeter of the vanishing energy separations between these states. In particular, we extract two separate (vanishing) energy scales corresponding (i) to insert a vison line between the two ends of the cylinder and (ii) to pull out and freeze a spin at either end. We also investigate the relations between bulk and boundary properties and show that, for a bipartition of the cylinder, the boundary Hamiltonian defined on the edge can be written as a product of a highly nonlocal projector, which fundamentally depends upon boundary conditions, with an emergent (local) SU(2)-invariant one-dimensional (superfluid) t-J Hamiltonian, which arises due to the symmetry properties of the auxiliary spins at the edge. This multiplicative structure, a consequence of the disconnected topological sectors in the space of dimer lattice coverings, is characteristic of the topological nature of the states. For minimally entangled RVB states, it is shown that the entanglement spectrum, which reflects the properties of the (gapless or gapped) edge modes, is a subset of the spectrum of the local Hamiltonian, e.g., half of it for the kagome RVB state, providing a simple argument on the origin of the topological entanglement entropy $S_0 = -\ln 2$ of the $\mathbb{Z}_2$ spin liquid. We propose to use these features to probe topological phases in microscopic Hamiltonians, and some results are compared to existing density matrix renormalization group data.

DOI: 10.1103/PhysRevB.86.014404 PACS number(s): 75.10.Kt, 03.65.Ud, 03.67.−a, 71.10.−w

I. INTRODUCTION

Conventional ordering in condensed matter systems is traditionally associated to symmetry breaking and to the existence of a local order parameter (Landau theory). Topologically ordered phases of matter[1] offer completely new classes of systems for which the ground-state (GS) degeneracy depends on topology (disk, cylinder, torus, etc.). The (short-range singlet) resonating valence bond (RVB) wave function proposed by Anderson[2] as the parent Mott insulator of high-temperature superconductors is a celebrated example. Such topological phases carry emerging fractionalized excitations and raise growing attention due to their potential to realize fault-tolerant setups for quantum computing.[3]

Experimental and theoretical search for topological liquids in quantum antiferromagnets[4] and in related microscopic models[5,6] has been a long-standing quest. One major problem is the existence of many possible (nonmagnetic) nearby competing states such as valence bond crystals[7] (spontaneously breaking lattice symmetry), clearly evidenced, e.g., in quantum dimer models.[8] Recent advances in the density matrix renormalization group (DMRG) techniques have reinforced the strong belief that a gapped spin liquid might be stabilized in the nearest-neighbor (NN) $S = 1/2$ Heisenberg quantum antiferromagnet (HAF).[9–12] This has also triggered the search for novel theoretical tools capable of better detecting topological order, in particular, entanglement measures used in quantum information. A common setup consists of dividing the system into two regions (named A and B) and compute the reduced density matrix (RDM) in the GS of, e.g., the A subsystem. The entanglement entropy (EE), defined as the von Neumann entropy of the RDM $S_{\mathrm{VN}} = -\rho_A \ln \rho_A$, contains an extensive term [proportional to the length of the boundary (area law)] and a universal subleading constant, the topological EE. Specific disklike setups[13] or cylindrical geometries can be used to extract the topological EE.

In fact, $-\ln \rho_A$ can be seen as a (dimensionless) Hamiltonian H_b, a key conceptual object. First, its spectrum, the so-called entanglement spectrum (ES), has been conjectured to show a one-to-one correspondence with the spectrum of edge states. This remarkable property was first established in fractional quantum Hall states[14] and, then, in quantum spin systems.[15] Furthermore, projected engangled pair states[16] (PEPS) offer a natural formulation of the relation between bulk and boundary. In Ref. 17, an explicit isometry was constructed which maps the Hamiltonian H_b onto another one $\tilde{H}_b$ acting on the space of auxiliary spins living at the edge of region A, while keeping the spectrum. Furthermore, for various two-dimensional (2D) models displaying quantum phase transitions, such as a deformed Affleck-Kennedy-Lieb-Tasaki (AKLT) (Ref. 18) or an Ising-type[19] model, it was found[17] that a gapped bulk phase with local order corresponds to a boundary Hamiltonian with local interactions, whereas critical behavior in the bulk is reflected in a diverging interaction length of $\tilde{H}_b$.

Entanglement properties of 2D topological phases are less well understood. Rokhsar-Kivelson (RK) wave functions,

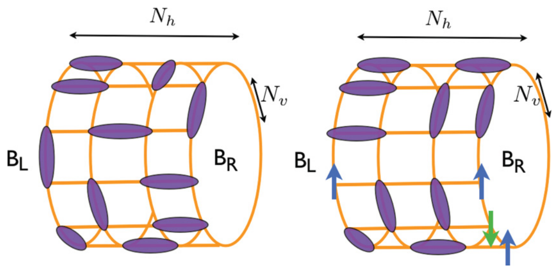

FIG. 1. (Color online) Typical valence bond configurations on a $N_v \times N_h$ cylinder with periodic boundary conditions along the vertical (v) direction. Ellipses represent singlets of two spins 1/2. Open (a) or generalized (b) boundary conditions on the B_L and B_R ends of the cylinder are considered (GBC can be obtained physically by freezing some spins at the boundaries, e.g., with local magnetic fields). The RVB wave function is defined as the equal-weight superposition of all such configurations (for a fixed realization of B_L and B_R).

defined as equal-weight superposition of fully packed dimer coverings, exhibit critical behavior on bipartite lattices[20] or realize the simplest topological phase, the so-called $\mathbb{Z}_2$ liquid, on frustrated lattices.[21] The topological EE of critical and topological RK wave functions have been computed using various topologies,[22] and the boundary Hamiltonian corresponding to the GS of Kitaev's toric code[3] was shown to be *nonlocal*.[17] Unfortunately, RK-type wave functions are not generic (their ES is completely dispersionless[23]) and do not describe real quantum $S = 1/2$ spin systems.[24,25] In contrast, (short-range) RVB states, defined as linear superposition of hard-core coverings of *nonorthogonal* nearest-neighbor SU(2) *singlets* [see Fig. 1(a)], appear to be closer to physical systems. Very recently, the (Renyi) EE between (finite) cylindrical regions has been computed[27] numerically for the critical[28,29] RVB state on the square lattice. Similarly, the (Renyi) topological EE of SU(2)-symmetric gapped chiral and $\mathbb{Z}_2$ spin liquids was obtained[30] using Kitaev-Preskill prescription. Nevertheless, ES and boundary Hamiltonians of such RVB/spin liquids wave functions are unknown.

In this work, we study topological and entanglement properties of both critical (square lattice) and gapped topologically ordered (kagome lattice) RVB wave functions[29] on *infinite* cylinders making use of simple PEPS representations. Let us describe here the organization of the paper: First, in Sec. II, we introduce RVB wave functions defined in the space of dimer (hard-core) coverings of square and kagome lattices. On cylinders with generalized boundary conditions, we review the construction of four disconnected topological sectors of dimer coverings (on the kagome lattice). Next, in Sec. III, we introduce the PEPS representation of the RVB wave functions and, making use of the disconnected topological sectors, explicitly construct four orthogonal RVB states. Using the quantum Heisenberg model as a reference Hamiltonian, we obtain the generic behavior of their energy splittings versus cylinder perimeter. In Sec. IV, we introduce a partition of the cylinder and compute the corresponding reduced density matrix (RDM). The (Hermitian) operator defined as minus the logarithm of the RDM can be viewed as a boundary Hamiltonian: it can be naturally expressed in the PEPS formalism as an operator acting on the virtual indices on the edges (up to an isometry). We show that the boundary Hamiltonian can be written as a product of a highly nonlocal projector, which depends fundamentally on the boundary conditions, by a local one-dimensional t-J model, which arises due to the symmetry properties of the auxiliary spins at the boundary and characterizes the (gapless or gapped) edge modes. This multiplicative structure is a direct consequence of the disconnected topological sectors in the space of dimer coverings of the lattice and, therefore, reflects the topological nature of the states. For sake of conciseness, more technical issues such as finite-size scalings, etc., are treated in Appendixes.

II. RVB WAVE FUNCTIONS ON CYLINDERS

A. Setup and boundary conditions

Let us first start with a square lattice on a cylinder of length N_h and circumference N_v with open boundary conditions (OBC) as depicted in Fig. 1(a). We consider the space of all nearest-neighbor $|\uparrow\downarrow\rangle - |\downarrow\uparrow\rangle$ singlet coverings of the lattice in such a way that each site belongs to one and only one dimer (so called "hard-core" coverings). Note that all singlets are oriented from one sublattice to the other. The resonating valence bond state is then defined as the equal-weight superposition of all such dimer (singlet) coverings. Aside from OBC, we also consider generalized boundary conditions (GBC) as in Fig. 1(b) by freezing some spins at the two boundaries B_L and B_R of the cylinder: in that case, dimers can not involve these "frozen" sites any more. Because of the local hard-core constraints, the choice of the boundary conditions will affect the physics in the center of the cylinder, even in the limit of an infinitely long one. Similar dimer coverings and RVB wave functions can be considered on cylinders with a kagome lattice (see, e.g., Fig. 2). In that case, singlets are all oriented clockwise in both left and right

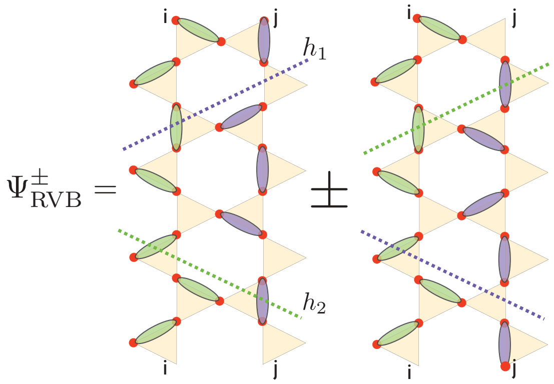

FIG. 2. (Color online) Two valence bond configurations on a 4×2 cylinder ($N_v = 4$). The two configurations are obtained from each other by translating all dimers (in purple) along a (single) closed loop encircling the cylinder. Such configurations can be distinguished from the parities $G_h = \pm 1$ of the number of dimers cut by *open* lines along the h_1 and h_2 directions joining the two B_L and B_R ends of the cylinder and, hence, define two different topological sectors. Two RVB (variational) ground states with $\langle G_h \rangle = 0$ can be constructed as equal-weight superpositions of all dimer coverings with + or − relative signs between the two topological sectors.

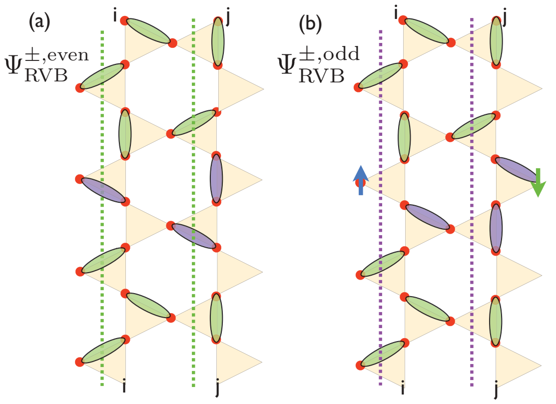

FIG. 3. (Color online) Two valence bond configurations on a 4 × 2 cylinder ($N_v = 4$ even). The two configurations are obtained from each other by translating all dimers (in purple) along a (single) *open* loop joining the two B_L and B_R ends of the cylinder (and adding extra spins). Such configurations can be distinguished from the parity $G_v = \pm 1$ of the number of dimers cut by any *closed* loop winding around the cylinder along the vertical direction and, hence, define two different "even" and "odd" topological sectors (and the corresponding RVB states).

triangles. It is known that RVB wave functions always exhibit short-range spin-spin correlations in two dimensions (2D) although dimer-dimer correlations can be either short range (kagome) or critical (square lattice) as mentioned above.

B. Topological sectors

Here, we briefly review the crucial concept of topological sectors in the space of (hard-core) dimer coverings (focusing on the kagome lattice) and show that four RVB wave functions belonging to different topological sectors can be constructed on $N_v \times N_h$ cylinders with periodic (open and generalized) boundary conditions in the vertical (horizontal) direction when N_v is even. The case of odd perimeter will also be discussed. For illustration, small 4 × 2 and 3 × 2 cylinders are drawn for simplicity in Figs. 2, 3, and 4, but our arguments are valid for any system size.

Let us first consider the case of a cylinder with N_v even. Topological sectors can be defined by considering (i) a closed loop in the vertical direction winding around the cylinder (see Fig. 2) and (ii) two open lines along the crystal directions h_1 and h_2 at 30° angles w.r.t. the horizontal axis (see Fig. 3), joining the two open ends B_L and B_R of the cylinder. As shown in Figs. 2 and 3, for a given configuration, the parities of the numbers of dimers cut by these loops are conserved quantities under translation of the vertical loop (horizontal lines) along the horizontal direction (vertical direction). Since the product of the three parities is constrained to be either even or odd (depending on the choice of N_h and N_v), NN dimer configurations can be grouped into four disconnected sectors. They are "topological" in nature since any *local* Hamiltonian acting on the space of dimer configurations preserves the sectors.

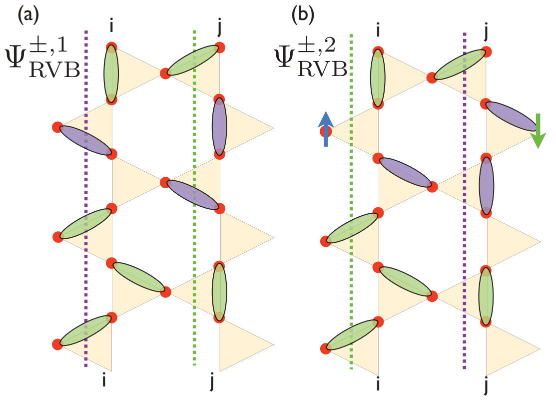

FIG. 4. (Color online) Same as Fig. 3 for a 3 × 2 cylinder ($N_v = 3$ odd).

It is interesting to note that one can go from one topological sector to the other by *nonlocal* moves of dimers. For example, let us consider the left configuration of Fig. 3. By translating any staggered arrangement of dimers around a closed loop winding around the cylinder by one lattice spacing, one permutes (changes) the parities G_h measured along h_1 and h_2 for $N_h = 4p + 2$ ($N_h = 4p$). Because the space of NN dimer coverings is divided into two disconnected sectors (fixing OBC), two RVB states can first be constructed separately in each sector. Such states should have the same energy density in the middle of the cylinder [for a generic local SU(2) Hamiltonian] since nothing can distinguish the two states locally. However, on a *finite* cylinder, such RVB states do not have the lowest variational energy since they break the mirror symmetry w.r.t. the horizontal direction (a symmetry assumed for the Hamiltonian) when $N_h = 4p + 2$. However, by taking their superpositions both with relative plus or minus signs (see Fig. 2), two appropriate variational GS $\Psi^+_{\rm RVB}$ and $\Psi^-_{\rm RVB}$ can be defined (strictly orthogonal for $N_h = 4p + 2$). Interestingly, starting from $\Psi^+_{\rm RVB}$, one can pictorially obtain $\Psi^-_{\rm RVB}$ by inserting a "vison" line going all the way from the left to the right boundaries of the cylinder, e.g., along the h_1 direction: the vison operator counts the number of dimers cut by the line and adds a minus sign to the wave function for an odd number of cuts. In other words, the $\Psi^+_{\rm RVB}$ (no vison) and $\Psi^-_{\rm RVB}$ (vison) are states with a *definite* $\mathbb{Z}_2$ flux through the cylinder.

The two states $\Psi^+_{\rm RVB}$ and $\Psi^-_{\rm RVB}$ have been constructed for specific OBC for B_L and B_R. Shifting by one lattice spacing a line of staggered dimers joining the two ends of the cylinder will change the parity G_v of the numbers of dimers cut by loops winding around the cylinder, hence providing a change from, say, the "even" to the "odd" topological sector, as seen in Fig. 3. By applying this second type of nonlocal move to the two previous $\Psi^+_{\rm RVB}$ and $\Psi^-_{\rm RVB}$ wave functions, one can then construct four orthogonal variational RVB wave functions denominated as $\Psi^{+,{\rm even}}_{\rm RVB}$, $\Psi^{-,{\rm odd}}_{\rm RVB}$, $\Psi^{+,{\rm even}}_{\rm RVB}$, and $\Psi^{-,{\rm odd}}_{\rm RVB}$.

Let us now briefly discuss the case of odd cylinders, i.e., cylinders with an odd number N_v of unit cells. As shown in Fig. 4, the parity of the number of dimers cut by *closed* loops encircling the cylinder along the vertical direction alternates along the cylinder. This indicates that two consecutive columns become nonequivalent and the system spontaneously dimerizes in the cylinder direction. By shifting a horizontal line of staggered dimers as before, one switches the parity of the even and odd columns. This defines two disconnected classes of configurations from which two related

RVB states $\Psi_{\rm RVB}^{+,1}$ and $\Psi_{\rm RVB}^{+,2}$ can be constructed as equal-weight superposition of all dimer configurations of each class. In the center of long (enough) cylinders, these two RVB states are simply related by a unit translation along the cylinder. Of course, as before, a vison line can be inserted between the two ends of the cylinder to derive two new $\Psi_{\rm RVB}^{-,1}$ and $\Psi_{\rm RVB}^{-,2}$ wave functions.

We finish this section with the case of the square lattice. Because of the much more constrained nature of dimer configurations on the square lattice, one can construct an extensive number $\propto N_v$ of topological sectors. This will be discussed in more details in Sec. IV.

III. PEPS REPRESENTATION OF RVB STATES

A. Mathematical construction

We start with the square lattice RVB wave function (NN $|\uparrow\downarrow\rangle - |\downarrow\uparrow\rangle$ singlets are all oriented from one sublattice to the other) on a cylinder of length N_h and circumference N_v, depicted in Figs. 5(a) and 5(c), corresponding to an equal-weight (and equal-sign) summation of all (singlet) dimer coverings. The RVB wave function can be expanded in the local S_z basis $|\Psi_{\rm RVB}\rangle = \sum_S c_S |s_1,s_2,\ldots,s_M\rangle$, where $s_n = 0,1$ are qubits (representing the two $S_z = \pm 1/2$ spin components) on the $M = N_h N_v$ sites and $S = \{s_n\}$. Such a state can in fact be represented by a $D = 3$ PEPS (Refs. 19 and 25) (up to local unitaries) where each lattice site is replaced by a rank-5 tensor $A^s_{\alpha,\alpha';\beta,\beta'}$ labeled by one physical index $s = 0$ or 1, and by four virtual bond indices (varying from 0 to 2) along the horizontal (α,α') and vertical (β,β') directions. Physically, the absence of singlet on a bond is encoded by the virtual index being "2" on that bond. To enforce the hard-core dimer constraint, one takes $A^s_{\alpha,\alpha';\beta,\beta'} = 1$ whenever three virtual indices equal 2 and the fourth one equals s, and $A^s_{\alpha,\alpha';\beta,\beta'} = 0$ otherwise. The amplitudes c_S are then obtained by contracting all virtual indices, except those at the ends of the cylinder fixed by boundary conditions, as depicted in Figs. 5(b) and 5(d). For the kagome lattice, as shown in Fig. 6, the RVB state can be represented in terms of rank-3 tensors (i) $A^s_{\alpha;\beta}$ on the sites–$A^s_{2;s} = A^s_{s;2} = 1$ and zero otherwise and (ii) on the center of each triangle $R_{2,2,2} = 1$, and $R_{\alpha,\beta,\gamma} = \epsilon_{\alpha\beta\gamma}$ otherwise, with $\epsilon_{\alpha\beta\gamma}$ the antisymmetric tensor.[25] One can then group the three sites on each unit cell to obtain a rank-5 tensor (the physical dimension is now $2^3 = 8$) connected on an effective square lattice [Figs. 6(b) and 6(c)]. Note that for the kagome PEPS, one can find a local parent Hamiltonian for which the degeneracy is equal to 4 on the torus.[25]

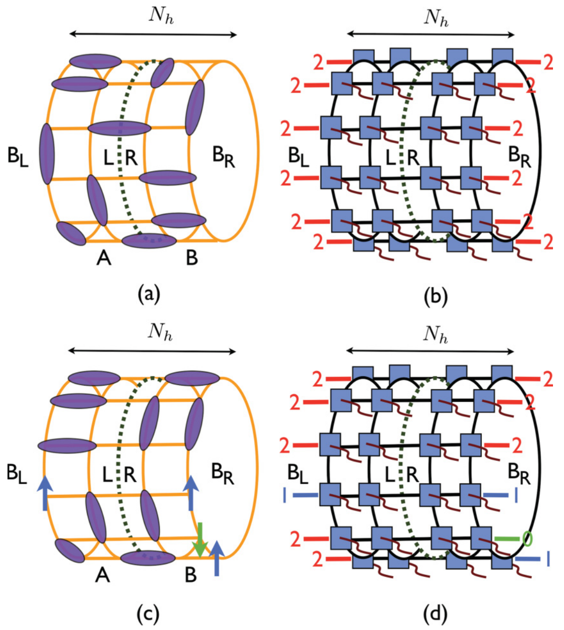

FIG. 5. (Color online) RVB wave functions on a cylindrical geometry: equal-weight superposition of hard-core dimer coverings [see, e.g., (a) and (c)] have simple representations in terms of PEPS [(b) and (d)]. The B_L and B_R boundary conditions of Figs. 1(a) and 1(b) can be realized by fixing the virtual variables going out of the cylinder ends; OBC (a) are defined by setting all boundary indices to "2" (b). Generalized boundary conditions (c) translate in the PEPS language by setting the boundary indices to 0 (spin ↓) or 1 (spin ↑) (d). A bipartition of the cylinder generates two L and R edges along the cut.

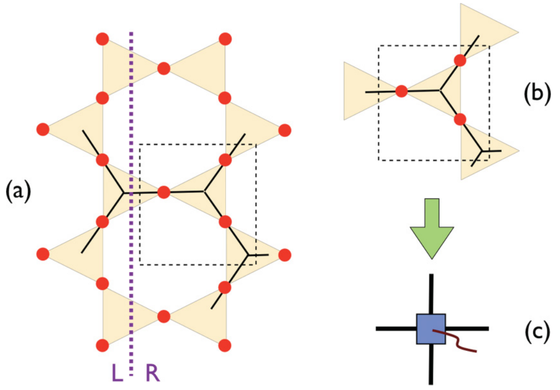

FIG. 6. (Color online) On the kagome lattice, an effective rank-5 tensor is constructed on each three-site unit cell. Three site tensors (red dots) carrying the physical indices and two 120° tensors (in the center of the shaded triangles) are grouped together (a), (b) to construct the basic tensor (c). The kagome lattice is then mapped onto an effective square lattice. A partition of the cylinder in the vertical direction generates L and R edges (thick dotted line).

In the PEPS formulation, the boundary conditions B_L and B_R can be simply set by fixing the virtual states on the bonds "sticking out" at each cylinder end. For example, open boundary conditions as in Fig. 5(a) are obtained by setting the boundary virtual indices to "2" as shown in Fig. 5(b). Generalized boundary conditions can be realized as in Figs. 5(c) and 5(d) by setting some of the virtual indices on the ends to 0 or 1.

B. Topological energy splittings of kagome RVB wave functions

More and more numerical data from DMRG simulations support the claim that the NN quantum HAF on the kagome lattice is a topological $\mathbb{Z}_2$ spin liquid.[9,11,12] It is therefore interesting (and relevant) to consider the previous topological NN-RVB wave functions as variational ground-state ansätze for the NN HAF Hamiltonian on the kagome lattice

$$H = J \sum_{\langle ij \rangle} \mathbf{S}_i \cdot \mathbf{S}_j\,, \qquad (1)$$

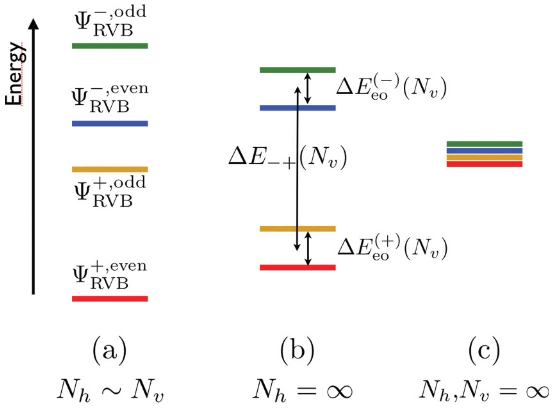

FIG. 7. (Color online) Illustration of the energy splitting between the four (variational) RVB wave functions for the kagome HAF. From left to right, the cylinder length (at fixed perimeter N_v even) and then its perimeter are increased to infinity.

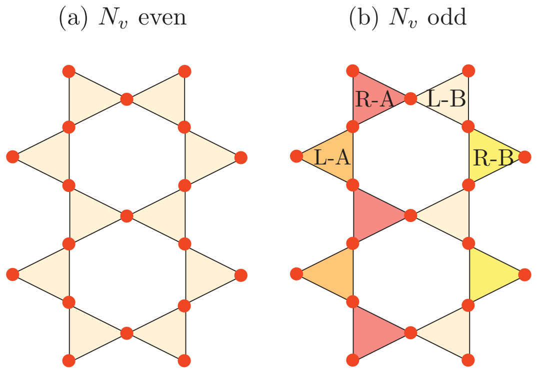

FIG. 8. (Color online) Schematic patterns of the exchange interaction on the triangles in the center of (quasi)infinite cylinders. For N_v even (N_v odd), the system is uniform (dimerized).

where $\mathbf{S_i}$ is the spin-$1/2$ operator at site i and $\langle ij\rangle$ stands for all NN bonds of the kagome lattice and the exchange constant has been set to $J=1$ from now on. Although (i) the (local) parent Hamiltonian of the NN-RVB wave function contains much more complicated interactions[25] and, conversely, (ii) the ground state of the NN HAF is far more involved that a simple NN-RVB (e.g., containing singlets bonds beyond NN), we believe generic features on the finite-size energy splitting between the different topological sectors (topological gap) can be obtained by using simple NN RVB wave functions. A schematic picture in Fig. 7 illustrates the expected GS multiplet structure for increasing system size. In the 2D thermodynamic limit, when both cylinder length and perimeter are infinite, one expects all energy splittings to vanish and the GS to become fourfold degenerate.

The PEPS formalism allows us to compute exactly the variational energy of the NN RVB wave functions on cylinders of perimeter N_v up to $N_v=10$ and length $N_h\to\infty$. $\Psi_{\mathrm{RVB}}^{+,\mathrm{even}}$ is obtained using the local rank-5 tensors described above and OBC. To get $\Psi_{\mathrm{RVB}}^{-,\mathrm{even}}$, one inserts a "vison" line joining the two boundaries of the cylinder by putting a string of $Z=\mathrm{diag}(1,1,-1)$ operators on the bonds.[26] Finally, $\Psi_{\mathrm{RVB}}^{\pm,\mathrm{odd}}$ are obtained by using GBC for B_L and B_R. The energy is computed at the center of the cylinder after full convergence with increasing cylinder length N_h is reached (typically, $N_h\sim 10N_v$ is enough). We have checked numerically that all states possess mirror symmetry of the energy density w.r.t. the horizontal axis (as expected from their symmetry) and are uniform (staggered) for N_v even (odd) as illustrated in Fig. 8. Interestingly, for $N_v=8$ and 10, the lattice C_{6v} symmetry around a hexagon center is almost fully recovered (i.e., the vertical and 30° bonds become equivalent). The energy (per site) of the four orthogonal RVB wave functions is plotted in Fig. 9(a) versus $1/N_v$. After averaging the energies of the even and odd states, one obtains very accurate fits of the exponentially fast convergence of the energies of the RVB wave functions in the "+" and "−" topological sectors, with a very short characteristic length scale $\xi_E\sim 1.0$. The extrapolated energy agrees very well with a recent estimate based on a Gutzwiller-projected superconducting wave function.[31] Although this variational energy is much higher than most recent variational estimates[9,11,12] (between -0.437 and -0.439), we believe the observed finite-size behaviors and energy splittings (topological gaps) should be generic of $\mathbb{Z}_2$ spin liquids. For example, we find that the average over the variational energies of the four RVB

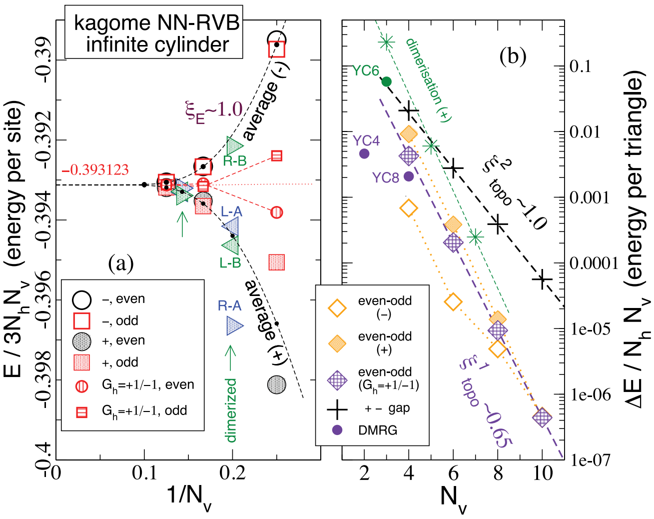

FIG. 9. (Color online) (a) Finite-size scaling of the energy (per site) of the four RVB wave functions on infinite kagome cylinders versus inverse perimeter N_v. 'Even" and "odd" refer to the parity of the number of spins frozen on the cylinder boundaries. "+" and "−" states differ by the absence or presence of a vison horizontal line, respectively. The energies of the fixed parity ($G_h=\pm1$) states are obtained by averaging the + and − energies (since the cross terms vanish) separately in the even and odd sectors. The energies of the four nonequivalent triangles of odd-perimeter infinite cylinders (with no vison) are also included. Averages over the even and odd energies separately in the no-vison (+) and vison (−) sectors are also shown. (b) Corresponding energy splittings (normalized per three-site unit cell) vs N_v [see Fig. 7(b)]. We also include the dimerization energy of the $\Psi_{\mathrm{RVB}}^{+,1,2}$ states on odd-perimeter infinite cylinders, defined as the energy difference between even and odd columns. DMRG data (S. R. White, Ref. 9 and private communication) for the dimerization of the YC6 cluster ($N_v=3$) or the spittings of the YC4 ($N_v=2$) and YC8 ($N_v=4$) clusters are shown for comparison. Dashed straight lines correspond to exponential fits of the form $A_0\exp(-N_v/\xi)$.

wave functions exhibits surprisingly small size dependence, in striking correspondence with DMRG results.[9,12]

The splittings between the variational RVB GS defined in Fig. 7(b) are plotted using a logarithmic scale in Fig. 9(b) as a function of the perimeter N_v of the infinite cylinder. Exponential decay of the topological splittings versus N_v are seen revealing *two* typical length scales $\xi^1_{\text{topo}} \sim 0.65$ and $\xi^2_{\text{topo}} \sim 1.01$, associated to the even-odd and $+/-$ gaps, respectively. Note that the dimerization energy of the $\Psi^{+,1}_{\text{RVB}}$ (or $\Psi^{+,2}_{\text{RVB}}$) states follows the same exponential decay as the even-odd topological gaps. For a very long cylinder with fixed boundary conditions, we therefore predict the following finite-size scaling of the largest topological splitting (cost of inserting a horizontal vison line)

$$\Delta E_{+-} \simeq 1.06\, N_v N_h \exp(-0.99\, N_v)\,. \tag{2}$$

The cost of freezing an *odd* number of spins at the boundary is given by

$$\Delta E_{eo} \simeq 1.95\, N_v N_h \exp(-1.54\, N_v) \tag{3}$$

for the case where the state has a definite parity ($G_h = \pm 1$). For a definite $\mathbb{Z}_2$ flux in the cylinder (e.g., a state with or without a vison), moderate corrections occur for perimeter $N_v \leqslant 8$ as seen in Fig. 9(b). In DMRG, the two different even and odd sectors can be fixed[9] by moving a site from one end of the cylinder to the other, which would be the same as pinning sites with strong fields on either end. However, it is not clear whether the DMRG algorithm chooses a definite G_h parity or a definite $\mathbb{Z}_2$ flux or neither of the two.

IV. BOUNDARY HAMILTONIAN ON INFINITE CYLINDERS

A. Bipartition and reduced density matrix

To define the boundary Hamiltonian of the RVB wave functions, we partition the $N_v \times N_h$ cylinder into two half-cylinders of lengths $N_h/2$, as depicted in Fig. 5. Partitioning the cylinder into two half-cylinders (playing the role of two A and B subsystems as defined in the Introduction) reveals two edges L and R along the cut. Ultimately, we aim to take the limit of infinite cylinders, i.e. $N_h \to \infty$ as before.

For a topological state, the boundary Hamiltonian depends on the choice of the wave function within the (variational) GS degenerate manifold. In other words, it depends upon (i) the choice of the B_L and B_R cylinder boundaries that impose the parity G_v (B_L and B_R have to "match") and (ii) the possible insertion of a horizontal vison line (or equivalently a $\mathbb{Z}_2$ flux through the cylinder). For simplicity, we restrict ourselves to the $+$ combination of Fig. 2 (no vison), but still consider arbitrary choices of the boundary conditions at the ends of the cylinder.

The boundary Hamiltonian $\tilde{H}_b$ can be derived from the reduced density operator $\sigma_b^2 = \exp(-\tilde{H}_b)$ acting on the edge indices, following the procedure given in Ref. 17. For the kagome lattice, there is no reflection symmetry w.r.t. the cut, so the RDM for the left (right) side takes the form $\sigma_{bL}^2 = \sqrt{\sigma_R^t}\,\sigma_L\sqrt{\sigma_R^t}$ ($\sigma_{bR}^2 = \sqrt{\sigma_L^t}\,\sigma_R\sqrt{\sigma_L^t}$) where σ_L and σ_R are obtained by contracting the tensors of the left and right half-cylinders, respectively, as shown in Fig. 10 (see Ref. 17 for details). Note that σ_{bL}^2 and σ_{bR}^2 give identical ES. For clarity, we restrict ourselves to σ_{bL}^2. Ultimately, we are interested in RVB cylinders with infinite lengths in both directions. First, we fix the cylinder perimeter ($N_v = 4,6,8$) and take the limit $N_h \to \infty$ as shown in Appendix A (in practice, the RDM for $N_h \sim 10 N_v$ is fully converged). The behaviors of the boundary Hamiltonian and the ES as a function of cylinder perimeter are then analyzed (see Appendix B for explicit finite-size scalings).

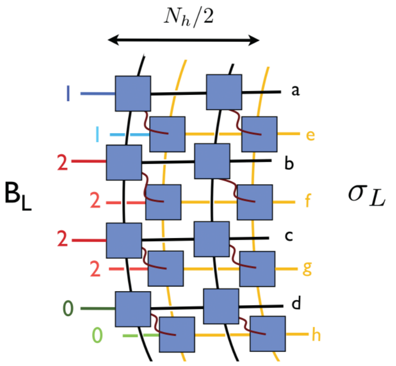

FIG. 10. (Color online) Boundary operator σ_L obtained by contracting all physical indices (wavy lines connecting the tensors in the front and in the back) of the left half-cylinder. Here, arbitrary boundary conditions have been chosen for B_L.

B. Boundary Hamiltonian

1. *Disconnected topological sectors in the PEPS representation*

The concept of boundary Hamiltonians is described in details in Ref. 17 and, for topological states, in Ref. 32. Here, we provide the details of their numerical computation for the RVB states. A crucial feature of the topological states is that the RDM depends intrinsically on the choice of the boundary conditions ($B_L = B_R$ for simplicity), *even when* $N_h \to \infty$. Indeed, the configurations of virtual indices (on the horizontal bonds) of any vertical column are split in two disjoined sectors which, due to local constraints, are conserved from column to column (and hence can be addressed independently from proper choices of $B_L = B_R$). This is directly connected to the partition of the space of NN dimer coverings into disconnected (even and odd for the kagome lattice) topological sectors discussed earlier. Indeed, the number of $|2\rangle$ states on a column of virtual bonds corresponds to the number of bonds with no dimers. Therefore, for the kagome lattice, in a given topological sector, the parity of the number of virtual $|2\rangle$ states on the columns is conserved from column to column. Consequently, the boundary Hamiltonian of the kagome RVB wave function conserves the parity of the number of $|2\rangle$ states, as in Kitaev's toric code. On the square lattice, extra constraints impose the conservation of the difference between the number of $|2\rangle$ states between two alternating sublattices on the edge. Hence, although the RDM (and $\tilde{H}_b$) acts on all 3^{N_v} degrees of freedom of the L (or R) edge, in each sector it contains a finite fraction of zero-weight eigenvalues, i.e., a finite fraction of eigenstates of $\tilde{H}_b$ have infinite energy. Calling $\mathcal{P}$ the projector on the finite-energy subspace, we split $\tilde{H}_b$ as $\tilde{H}_b = H_1 + \beta_\infty(\text{Id} - \mathcal{P})$, where Id is the $3^{N_v} \times 3^{N_v}$ identity operator, $\beta_\infty \to \infty$, and H_1 is supported by the nonzero eigenvalues sector of the RDM. More precisely, H_1 can be factorized as $H_1 = H_{\rm local}\mathcal{P}$ where $H_{\rm local}$ is a Hamiltonian (shown later to be local) acting on the whole boundary space,[33] commuting with $\mathcal{P}$ and *independent on BC*. The kagome cylinder has only two sectors defined by $\mathcal{P} = P_{\rm even}$ and $\mathcal{P} = \mathcal{P}_{\rm odd} = {\rm Id} - P_{\rm even}$, which can be obtained by choosing an even or odd number of "2" external (virtual) indices for $B_L = B_R$, respectively. On the square lattice cylinder, there are $N_v + 1$ disconnected sectors defined by projectors $\mathcal{P}_\Delta$ enforcing a fixed difference $N_{2,X} - N_{2,Y} = \Delta$ of the numbers of "2" on two X and Y alternating sublattices on the edge, $\Delta = -N_v/2,\dots,N_v/2$. The fact that H_1 is known for all sectors implies that $H_{\rm local}$ is uniquely determined as will be shown in the next section.

2. Practical derivation of $H_{\rm local}$

In practice, each numerical calculation is done for a specific choice of the boundary conditions B_L and B_R (for simplicity, we assume here $B_L = B_R$) on the cylinder ends, which determines a given conserved sector (mathematically characterized by some projector $\mathcal{P}$), support of the corresponding boundary Hamiltonian. Conversely, all sectors (associated to different projectors $\mathcal{P}$) can be obtained from proper choices of the boundary conditions $B_L = B_R$ (like the sectors defined by the projectors $\mathcal{P}_{\rm even}$ and $\mathcal{P}_0$ which can be addressed by choosing OBC).

On the kagome cylinder, the two sectors defined by $\mathcal{P} = P_{\rm even}$ and $\mathcal{P} = \mathcal{P}_{\rm odd} = \mathbf{1}^{\otimes N_v} - P_{\rm even}$ can be obtained by choosing even (e.g., OBC) or odd number of "2" external (virtual) indices on both the left and right boundaries of the cylinder, respectively. We can then construct a "mixed" RDM (for the right part)

$$\sigma_b^2 = \sqrt{\sigma_L^{\,t}}\,\sigma_R\sqrt{\sigma_L^{\,t}} \tag{4}$$

by considering the linear superpositions

$$\begin{aligned}\sigma_R &= \sigma_{R,\rm even} + \sigma_{R,\rm odd},\\ \sigma_L &= \sigma_{L,\rm even} + \sigma_{L,\rm odd},\end{aligned} \tag{5}$$

where $\sigma_{T,\rm p}$ are obtained by contracting the left ($T = L$) and right ($T = R$) half-cylinders (see Ref. 17) with appropriate $p = $ even or $p = $ odd parity boundary conditions and the equal-weight normalization condition

$$\mathrm{Tr}\{(\sigma_{L,\rm even})^t\sigma_{R,\rm even}\} = \mathrm{Tr}\{(\sigma_{L,\rm odd})^t\sigma_{R,\rm odd}\} = 1. \tag{6}$$

Since $\sigma_{T,\rm even}$ and $\sigma_{T,\rm odd}$ are supported on disconnected subspaces, the mixed RDM splits into orthogonal contributions $\sigma_b^2 = \rho_{\rm even} + \rho_{\rm odd}$, where

$$\begin{aligned}\rho_{\rm even} &= \sqrt{\sigma^{\,t}_{L,\rm even}}\,\sigma_{R,\rm even}\sqrt{\sigma^{\,t}_{L,\rm even}}\,,\\ \rho_{\rm odd} &= \sqrt{\sigma^{\,t}_{L,\rm odd}}\,\sigma_{R,\rm odd}\sqrt{\sigma^{\,t}_{L,\rm odd}}\,.\end{aligned} \tag{7}$$

Since σ_b^2 is supported by the whole Hilbert space, $H_{\rm local}$ can be *uniquely* defined by setting $\sigma_b^2 = \exp(-H_{\rm local})$, enabling a direct computation of $H_{\rm local} = -\ln\sigma_b^2$ from Eqs. (4) and (5). Conversely, the generic form of the boundary Hamiltonian associated to the (normalized) RDM ρ_p is given by

$$\tilde{H}_b = H_{\rm local}\mathcal{P}_p + \beta_\infty\mathcal{P}_{\bar p}\,, \tag{8}$$

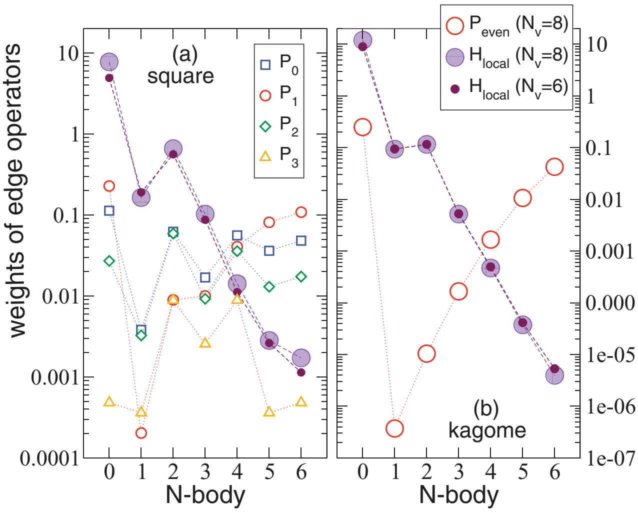

FIG. 11. (Color online) Weights of the projectors $\mathcal{P}_\Delta$, $\Delta = 0,1,2,$ and 3 (square lattice, $N_v = 6$) and $\mathcal{P}_{\rm even}$ (kagome lattice, $N_v = 8$) expended in terms of N-body operators. Same for $H_{\rm local}$ for the RVB wave function on the square (a) and kagome (b) lattices, on $N_v = 6$ (small symbols) and $N_v = 8$ (large symbols) infinite cylinders.

with $\beta_\infty \to \infty$ and where p ($\bar p$) refers to the even (odd) or odd (even) parity sector.

For the RVB wave function on the square lattice, there are $N_v/2 + 1$ orthogonal sectors defined by the projectors $\mathcal{P}_\Delta$ enforcing a fixed difference $|N_{2,A} - N_{2,B}| = \Delta$ on the two A and B alternating sublattices on the one-dimensional edge, $\Delta = 0,1,\dots,N_v/2$. We show (for $N_v = 6$) the expansion of these projectors in terms of N-body operators in Fig. 11(a), highlighting clearly their highly nonlocal character. We construct the "mixed" RDM σ_b^2 from the linear superposition

$$\sigma_b = \sum_{\Delta=0}^{N_v/2}\sigma_\Delta\,, \tag{9}$$

where σ_Δ is obtained by contracting the infinite (left or right) half-cylinder (see Ref. 17) with appropriate boundary conditions and normalized according to $\mathrm{Tr}(\sigma_\Delta^2) = 1$. The operators σ_Δ are supported on orthogonal subspaces which span the whole space of virtual indices on the edge, i.e., $\sum_\Delta\mathcal{P}_\Delta = \mathbf{1}^{\otimes N_v}$. Therefore, since σ_b^2 lives on the whole Hilbert space of the edge, one can *uniquely* define $H_{\rm local}$ as $H_{\rm local} = -\ln\sigma_b^2$. Consequently, $H_{\rm local}$ can be computed numerically using Eq. (9). It also follows that, for each sector, the corresponding boundary Hamiltonian is

$$\tilde{H}_b = H_{\rm local}\mathcal{P}_\Delta + \beta_\infty\bar{\mathcal{P}}_\Delta\,, \tag{10}$$

with $\beta_\infty \to \infty$ and $\bar{\mathcal{P}}_\Delta = \mathbf{1}^{\otimes N_v} - \mathcal{P}_\Delta$ is the projector on the complementary subspace.

3. Expansion in terms of N-body operators: Numerical results

Next, we wish to explore the nonlocal/local characters of the $H_1/H_{\rm local}$ edge operators. Any operator $\mathcal{O}_{\rm edge}$ acting on the edge can be expanded in terms of 3^{2N_v} orthogonal operators. For this purpose, we use a local basis of 9 (normalized) operators $\{\hat{x}_0,\dots,\hat{x}_8\}$ which act on the local basis of configuration (at some site i) $\{|0\rangle,|1\rangle,|2\rangle\}$, e.g., $\hat{x}_0 =$

1, $\hat{x}_1 = \sqrt{\frac{3}{2}}(|0\rangle\langle 0| - |1\rangle\langle 1|)$, and $\hat{x}_2 = \frac{1}{\sqrt{2}}(|0\rangle\langle 0| + |1\rangle\langle 1| - 2|2\rangle\langle 2|)$, for the diagonal matrices, complemented by $\hat{x}_3 = \hat{x}_4^\dagger = \sqrt{3}|0\rangle\langle 1|$ acting as "spin" operators, and $\hat{x}_5 = \hat{x}_7^\dagger = \sqrt{3}|2\rangle\langle 0|$ and $\hat{x}_6 = \hat{x}_8^\dagger = \sqrt{3}|2\rangle\langle 1|$ acting as annihilation and creation (hard-core) bosonic operators.[35] The expansion in terms of N-body operators reads as (see Appendix C for more details)

$$\mathcal{O}_{\text{edge}} = c_0 N_v + \sum_{\lambda,i} c_\lambda \hat{x}_\lambda^i + \sum_{\lambda,\mu,r,i} d_{\lambda\mu}(r)\,\hat{x}_\lambda^i \hat{x}_\mu^{i+r} + \sum_{\lambda,\mu,\nu,r,r',i} e_{\lambda\mu\nu}(r,r')\,\hat{x}_\lambda^i \hat{x}_\mu^{i+r} \hat{x}_\nu^{i+r'} + \dots, \qquad (11)$$

where each group of terms involves products of N ($1 \leqslant N \leqslant N_v$) onsite $\hat{x}_\lambda$ ($\lambda \neq 0$) operators. Here, the sums are restricted to nonequivalent relative distances and only translations giving *distinct* sets of sites are performed. The (real) coefficients appearing in (11) have been computed for $\mathcal{O}_{\text{edge}} = \mathcal{P}_{\text{even}}$ (kagome lattice), $\mathcal{O}_{\text{edge}} = \mathcal{P}_\Delta$ (square lattice), and $\mathcal{O}_{\text{edge}} = H_{\text{local}}$ (kagome and square lattices) on infinitely long cylinders of perimeters $N_v = 6$ and 8 up to order $N = 6$.

As seen from the distribution of their weights in Figs. 11(a) and 11(b), projectors are highly nonlocal, conferring a fundamentally nonlocal character to the boundary Hamiltonian H_1. This is also to be expected for *realistic* topological GS of microscopic Hamiltonians on geometries involving open or fixed BC in some directions.

The total weights corresponding to each order of the expansion of H_{local} in terms of N-body operators are shown in Figs. 11(a) and 11(b) as a function of the order N. Finite-size effects are remarkably small, and we believe the results for $N_v = 8$ are converged. The data reveal clearly an exponential decay of the weight with the order N. In other words, H_{local} contains primarily one- and two-body contributions (in addition to the the normalization constant). This is the first part of the proof that H_{local} is indeed local. However, one still needs to go beyond the analysis and investigate further the r dependence of the leading two-body contributions. In the next section, we show that H_{local} of the $\mathbb{Z}_2$ topological RVB is basically a short-range two-body Hamiltonian. In contrast, the RVB wave function on the square lattice exhibits a long-range two-body potential term.

4. *Local boundary Hamiltonian: An effective one-dimensional t-J model*

Next, we investigate the exact connection between the boundary Hamiltonian and the bulk properties of the system. We look for its explicit form, trying to make the connection with $D = 3$ models, with SU(2) symmetry corresponding to the $1/2 \oplus 0$ representation.

The boundary Hamiltonian belongs to the $1/2 \oplus 0$ representation of SU(2) and its Hilbert space is the same as the one of a *bosonic* t-J model. Therefore, H_{local} is formally equivalent to a one-dimensional (1D) "t-J model"[36] describing motion of (bosonic) "holes" (the "2") in a spin-fluctuating background (the "0" and "1" qubits) supplemented by additional density-density and pair-field terms, conferring a superfluid character to the edge. One can then rewrite the previous local operators in the notations of the 1D t-J model.[36] We define bosonic creator operators $b_{i,s}^\dagger$ ($s = 0,1$) of the $|0\rangle$ and $|1\rangle$ states from the "vacuum" $|2\rangle$ (at some site i) as $b_{i,s}^\dagger = |s\rangle\langle 2|$, which naturally enforce the local Gutzwiller constraint of no doubly occupied site (in terms of hard-core bosons), so we can identify, e.g., $b_{i,0} = \frac{1}{\sqrt{3}}\hat{x}_5$, $b_{i,1} = \frac{1}{\sqrt{3}}\hat{x}_6$, $b_{i,0}^\dagger = \frac{1}{\sqrt{3}}\hat{x}_7$, and $b_{i,1}^\dagger = \frac{1}{\sqrt{3}}\hat{x}_8$.

The form of the Hamiltonian components is dictated by the spin symmetry of the boundary Hamiltonian. We restrict here to the (dominant) one- and two-body terms of H_{local}. The unique one-body (diagonal) term can be written as a chemical potential term $\mathcal{H}_2$:

$$\sum_i \hat{x}_2^i = \frac{3}{\sqrt{2}} \sum_i (n_i - 2/3) = \frac{3}{\sqrt{2}} \mathcal{H}_2\,, \qquad (12)$$

where $n_i = n_{i,0} + n_{i,1}$ counts the number of 0 or 1 on site i. The diagonal two-body density-density operators take the form of a density-density (repulsive) interaction $\mathcal{H}_V$:

$$\sum_i \hat{x}_2^i \hat{x}_2^{i+r} = \frac{9}{2} \sum_i (n_i - 2/3)(n_{i+r} - 2/3) = \frac{9}{2}\,\mathcal{H}_V(r). \qquad (13)$$

Defining the pseudospin $\mathbf{S} = \frac{1}{2}\sum_{s,s' \in \{0,1\}} \vec{\sigma}_{ss'} |s\rangle\langle s'|$ involving a combination of $\hat{x}_1$, $\hat{x}_3 = \sqrt{3}|0\rangle\langle 1|$ and $\hat{x}_4 = \sqrt{3}|1\rangle\langle 0|$, and combining three two-body terms (that appear in H_1 and H_{local} with the same weights), we obtain an effective Heisenberg-type couplings $\mathcal{H}_J(r)$:

$$\sum_i \left(\hat{x}_1^i \hat{x}_1^{i+r} + \hat{x}_3^i \hat{x}_4^{i+r} + \hat{x}_4^i \hat{x}_3^{i+r}\right) = 6 \sum_i \mathbf{S}_i \cdot \mathbf{S}_{i+r} = 6\,\mathcal{H}_J(r)\,. \qquad (14)$$

By symmetry, one also gets (short-range) hopping terms $\mathcal{H}_t(r)$ by combining

$$\sum_i \left(\hat{x}_7^i \hat{x}_5^{i+r} + \hat{x}_5^i \hat{x}_7^{i+r} + \hat{x}_8^i \hat{x}_6^{i+r} + \hat{x}_6^i \hat{x}_8^{i+r}\right) = 3 \sum_{i,s} (b_{i+r,s}^\dagger b_{i,s} + b_{i,s}^\dagger b_{i+r,s}) = 3\,\mathcal{H}_t(r)\,, \qquad (15)$$

and Josephson couplings $\mathcal{H}_\Delta(r)$ by combining

$$\sum_i \left(\hat{x}_6^i \hat{x}_5^{i+r} - \hat{x}_5^i \hat{x}_6^{i+r} + \hat{x}_8^i \hat{x}_7^{i+r} - \hat{x}_7^i \hat{x}_8^{i+r}\right) = 3 \sum_i (b_{i,0} b_{i+r,1} - b_{i,1} b_{i+r,0}) + \text{H.c.} = 3\mathcal{H}_\Delta(r)\,, \qquad (16)$$

which describe fluctuations of (s-wave) short-range singlet pairs. The local Hamiltonian takes then the final form

$$H_{\text{local}} = c_0 N_v + \frac{3c_2}{\sqrt{2}} \mathcal{H}_2 + \sum_r V_r \mathcal{H}_V(r) + \sum_r t_r \mathcal{H}_t(r) + \sum_r J_r \mathcal{H}_J(r) + \sum_r \Delta_r \mathcal{H}_\Delta(r) + H_{\text{rest}}\,, \qquad (17)$$

where H_{rest} contains all negligible $N > 3$ contributions. The new physical parameters are simply related to the amplitudes appearing in the expansion (11) of H_{local}: $t_r = 3\,d_{57}(r) = 3\,d_{68}(r)$, $J_r = 6\,d_{11}(r) = 6\,d_{34}(r)$, $V_r = \frac{9}{2}\,d_{22}(r)$, and $\Delta_r = 3\,d_{65}(r) = 3\,d_{87}(r)$.

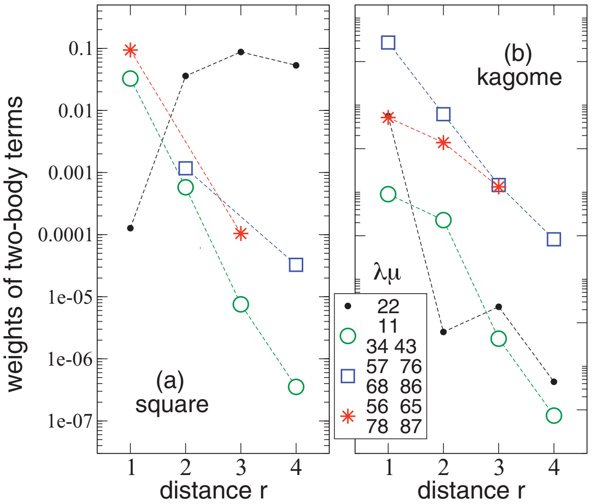

FIG. 12. (Color online) Weights $|d_{\lambda\mu}(r)|^2$ of the two-body operators appearing in H_{local} for the square (a) and kagome (b) lattices. In (a), the diagonal interaction $\hat{x}_2^i \hat{x}_2^{i+r}$ shows a long-range behavior.

For the $\mathbb{Z}_2$ RVB liquid on the kagome lattice, as seen on Fig. 12(b), all weights $d^2_{\lambda\mu}(r)$ (and hence all the physical parameters t_r, J_r, V_r, and Δ_r) decay exponentially fast with r so that H_{local} is a truly local operator. The dominant two-body contribution to H_{local} is the (negative) hopping term. The density-density interaction is attractive between nearest-neighbor sites ($V_1 < 0$), while it becomes repulsive (and very small) at longer distance ($V_r > 0$ for $r \geqslant 2$). Finally, we note that the small Heisenberg spin interaction is *ferromagnetic* at all distances ($J_r < 0$). For the critical RVB wave function on the square lattice, as seen on Fig. 12(a), all weights $d^2_{\lambda\mu}(r)$ also decay exponentially fast with r *except* the (diagonal) density-density interaction $\mathcal{H}_V(r)$, which remains long range. These remarkable features are to be connected to the bulk correlations of the RVB wave functions: short-range (critical) bulk correlations translate into short-range (long-range) boundary Hamiltonians. We have therefore established a one-to-one correspondence between the long-range behavior of the bulk correlations and the range of the boundary Hamiltonian of RVB wave functions. This extends the previous findings[17] to the case of topological order.

C. Entanglement spectra and edge modes

We now move to the investigation of the full bipartite ES, which is given by the spectrum of H_{local}. Our results are summarized in Figs. 13(a) and 13(b) and 14(a) and 14(b) for infinitely long cylinders with kagome and square lattices. For convenience, the GS energy of H_{local} (corresponding to the largest weight in the RDM) is subtracted from the spectra. The (excitation) ES are shown as a function of momentum around the cylinder and the eigenstates are labeled according to their spin-multiplet structure inherited from the SU(2) symmetry of the RVB state, although with the $1/2 \oplus 0$ representation.[34] A careful finite-size scaling (see Appendix B) suggests that the kagome (square) lattice cylinder ES is gapless (gapped) in the limit $N_v \to \infty$. Since these features are opposite to what is expected for the energy excitation spectra of the corresponding bulk systems (according to their long-wavelength properties), we deduce that the ES characterizes specifically the nature of the L and R edge modes (Fig. 1). Note that for given choice of BC, the actual ES is the spectrum of a *projected* H_1 Hamiltonian and, hence, is a subset of the full ES. For example, in a kagome lattice (square lattice) cylinder with OBC, a common setup in numerical simulations, only (a subset of) the integer spin eigenstates are obtained.

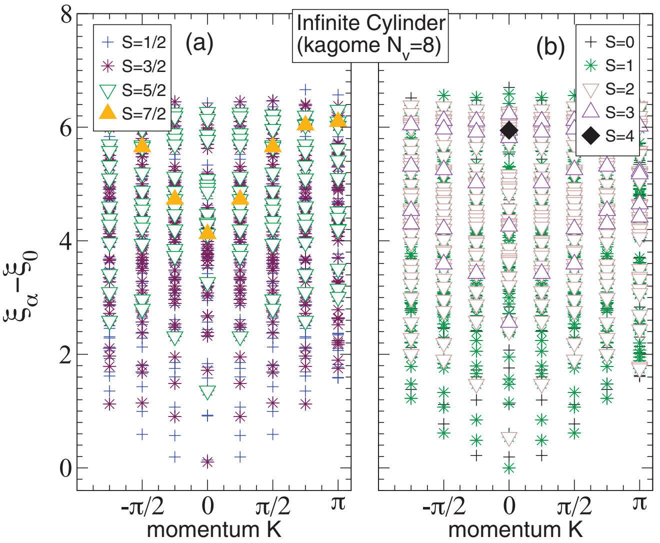

FIG. 13. (Color online) ES (w.r.t. the *same* $S_z = 0$ GS energy ξ_0 at $K = 0$) of an infinitely long kagome cylinder of perimeter $N_v = 8$. Eigenstates with half-integer (a) and integer (b) spins correspond to odd and even sectors, respectively (see text).

D. Topological entropy

It is of great interest to investigate the entanglement entropy which can give access to the quantum dimension $\mathcal{D}$ and hence provides clear fingerprints of topological order.[1] We recall that

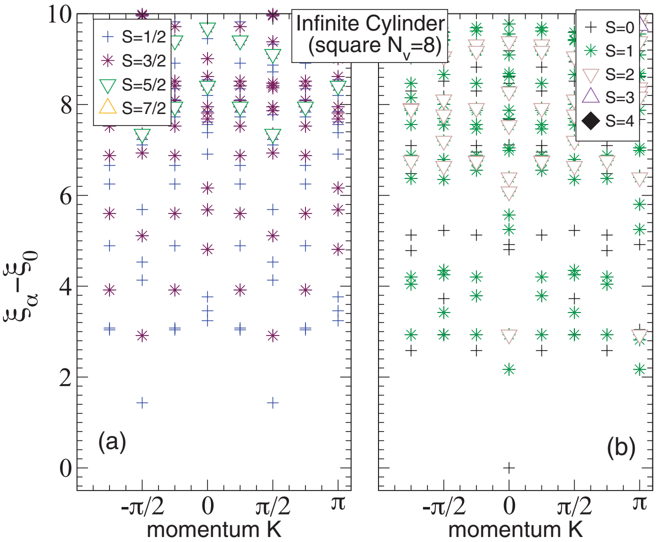

FIG. 14. (Color online) Same as Fig. 13 for the critical RVB state (square lattice). Eigenstates with half-integer (integer) spins correspond to Δ odd (even) (see text). For OBC, one gets a subset of (b) ($\Delta = 0$ sector).

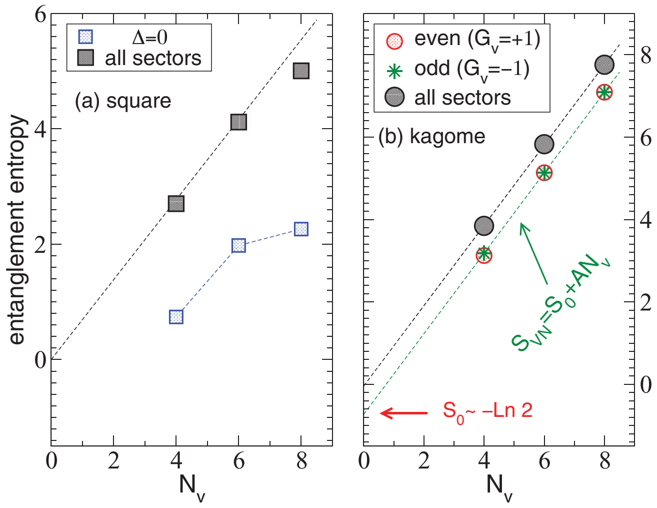

FIG. 15. (Color online) Entanglement entropy versus perimeter N_v for specific sectors (open symbols) or when summing over all sectors (shaded symbols). (a) Square lattice ($\Delta = 0$ is obtained with OBC); (b) kagome lattice (no $\mathbb{Z}_2$ flux through the cylinder, $G_h = 0$).

we consider here the RVB wave function for which the *same* sign enters in the linear superposition of the dimer coverings (defined, on the kagome lattice, as $\Psi^{+}_{\rm RVB}$ with no vison line, i.e., no $\mathbb{Z}_2$ flux through the cylinder). We investigate infinite cylinders and study the behavior of the EE as a function of the perimeter. From specific choices of the cylinder boundary conditions, we can select specific conserved sectors on the edge (e.g., OBC for the kagome cylinder selects the even sector, etc.). The EE is given by the von Neumann entropy $S_{\rm VN} = -{\rm Tr}\{\sigma_b^2 \ln \sigma_b^2\}$.

As shown in Fig. 15(a), the EE of the square lattice cylinder with OBC ($\Delta = 0$ sector) shows strong deviations from the area law (i.e., linear behavior with N_v) which should be connected to the critical nature of the RVB wave function. In contrast, for both even and odd (edge) sectors of the kagome RVB wave function, the EE can be well fitted according to $S_{\rm VN} = S_0 + AN_v$, where $S_0 = -\ln \mathcal{D}$ is the topological EE, as shown in Fig. 15(b). The existence of a finite S_0, a smoking gun of the topological nature of the RVB state, can be seen as a direct consequence of the particular structure of $H_{\rm l}$ according to the following argument: The EE is given (crudely) by $-\ln \mathcal{N}$ where $\mathcal{N}$ is the number of eigenstates of $H_{\rm l}$ below a fixed energy scale of order 1. For fixed cylinder boundaries, the support of $H_{\rm l} = H_{\rm local}\mathcal{P}$ ($\mathcal{P} = \mathcal{P}_{\rm even}$ or $\mathcal{P} = \mathcal{P}_{\rm odd}$) contains $\mathcal{N} \simeq \frac{1}{2}3^{Nv}$ states and $S_0 = -\ln 2$, as expected for a topological $\mathbb{Z}_2$ spin liquid with quantum dimension $\mathcal{D} = 2$. Note that $\Psi^{+,\rm even}_{\rm RVB}$ and $\Psi^{+,\rm odd}_{\rm RVB}$ can be seen as "minimally entangled states" naturally produced by the DMRG algorithm from amongst the quasidegenerate ground states of the $\mathbb{Z}_2$ topological phase.[11] Linear combination of them (or, e.g., of $\Psi^{+,\rm even}_{\rm RVB}$ and $\Psi^{-,\rm even}_{\rm RVB}$) should give a larger topological entropy.

Summing over all sectors amounts to taking $H_{\rm l} = H_{\rm local}$ so that all eigenstates of the ES contribute and $S_{\rm VN} \propto N_v$ (as can be shown rigorously) as seen in Fig. 15(b). For the square lattice, severe constraints lead to an *extensive* number (i.e., proportional to the perimeter N_v) of disconnected sectors on the edge of dimension $\mathcal{N} \simeq \frac{1}{N_v} 3^{Nv}$, therefore introducing *negative* logarithmic corrections $\sim -\ln N_v$ to the EE for any boundary conditions [see, e.g., data for OBC on Fig. 15(a)]. The long-range diagonal interaction in $H_{\rm local}$ [Fig. 12(a)] may also be responsible for deviations from the area law, even when considering all sectors.

V. DISCUSSION AND OUTLOOK

By introducing PEPS representations and using tensor networks techniques, we have examined topological and entanglement properties associated to gapped and gapless RVB states using cylindrical geometries with arbitrary boundary conditions. The formalism allows us to take the limit of infinite cylinders. Using the simple topological structure of the space of dimer coverings on the kagome lattice, we construct four quasidegenerate (for a generic quantum HAF) orthogonal RVB states and obtain the finite-size scalings of the energy splittings amongst them (topological gaps), which could be compared to numerical simulations. Incidentally, our results identify two very different energy splittings decaying with two clearly different length scales. The largest energy scale corresponds to inserting a (horizontal) vison line (or a $\mathbb{Z}_2$ flux in the cylinder). The second energy scale corresponds to pinning a site with a strong field on either end of the cylinder, which would be the same as moving a site from one end to the other. Although it has been suggested that the DMRG algorithm (naturally) selects a minimally entangled state,[11] it is still not clear how to reconcile the fact that the finite-size corrections of the ground-state energy are very small,[9,12] while our RVB computation predicts clear finite-size effects for the states with a definite $\mathbb{Z}_2$ flux. On the other hand, we find that the energy *averaged* over the four (minimally entangled) RVB states shows very small finite-size effects.

In addition, we show that boundary Hamiltonians can be written as $H_{\rm local}\mathcal{P} + \beta_{\rm topo}({\rm Id} - \mathcal{P})$, $\beta_{\rm topo} \to \infty$. In particular, we have established the existence of a projector $\mathcal{P}$ (which intrinsically depends on the boundary conditions) onto a restricted subspace at the edge (as for Kitaev toric code[3,17]), a consequence of the disconnected topological sectors in the space of dimer coverings of the lattice. We argue that the nonlocal character of the resulting boundary Hamiltonian is the fingerprint of topology. The ES is a subset (associated to $\mathcal{P}$) of the spectrum of the emerging local Hamiltonian $H_{\rm local}$ acting on the unrestricted edge space. In contrast to the toric code for which $H_{\rm local}$ is trivial, here $H_{\rm local}$ takes the form of a short-range (bosonic) t-J model (including a long-range diagonal interaction for the critical RVB state). We argue that the topological features (e.g., finite-size scaling of topological gaps) and entanglement properties (e.g., structure of boundary Hamiltonians) of the NN RVB wave functions are characteristic of topological phases. We propose to use these features to detect topological order in microscopic models.[6,9–12]

ACKNOWLEDGMENTS

D.P. acknowledges support by the "Agence Nationale de la Recherche" under Grant No. ANR 2010 BLANC 0406-0. This work was granted access to the HPC resources of CALMIP under the allocation 2012-P1231. D.P. also thanks S. R. White

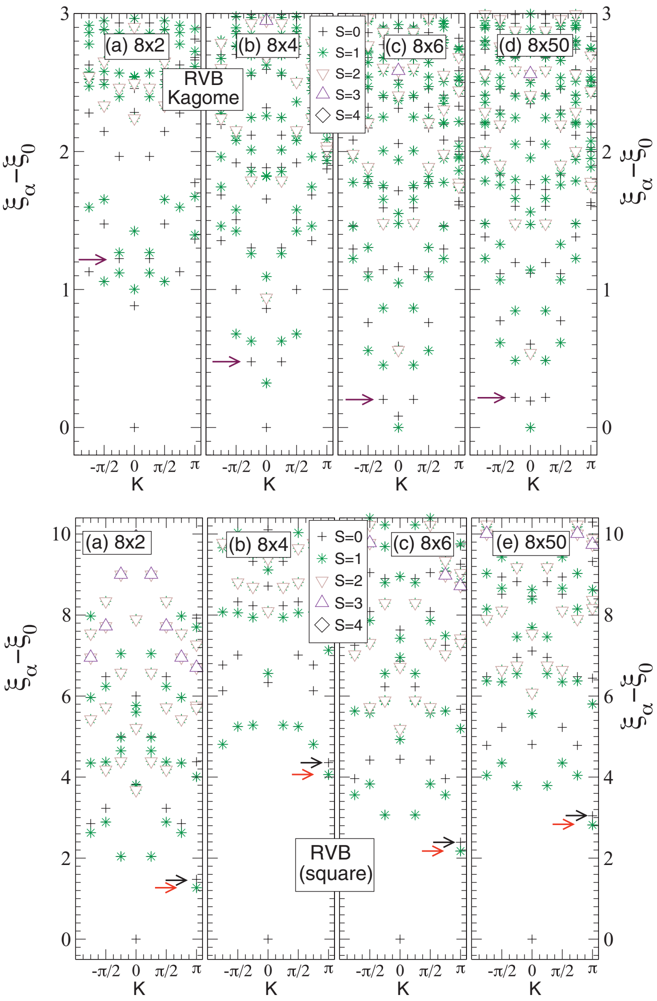

FIG. 16. (Color online) ES of a cylinder with fixed perimeter $N_v = 8$ and increasing length N_h ranging from 2 to 50. OBC are used for B_L and B_R. Kagome (top) and square (bottom) lattices.

for sharing DMRG results and S. A. Kivelson for useful correspondence. N.S. acknowledges helpful discussions with F. Verstraete and support by the Alexander von Humboldt foundation, the Institute for Quantum Information and Matter (an NSF Physics Frontiers Center with support of the Gordon and Betty Moore Foundation), and the NSF Grant No. PHY-0803371. D.P.-G. acknowledges QUEVADIS and Spanish grants QUITEMAD and MTM2011-26912. J.I.C. acknowledges the EC project Quevadis, the DFG Forschergruppe 635, and Caixa Manresa. This work was initiated at Centro de Ciencias Pedro Pascual (Benasque, Spain).

APPENDIX A: TAKING THE LIMIT OF THE INFINITE CYLINDER

The (excitation) ES is shown in Fig. 16 as a function of momentum around the cylinder and the eigenstates are labeled according to their spin-multiplet structure inherited from the SU(2) symmetry of the RVB state, although with the $1/2 \oplus 0$ representation. From the data shown in Fig. 16, we see that, for a fixed perimeter, the ES converges rapidly when increasing the length towards the infinite-cylinder limit ($N_h = \infty$). The latter is reached as soon as $N_h > N_v$ ($N_h \gg N_v$) for the kagome (square) lattice: in practice, the RDM for $N_h = 50$ is fully converged. This is clear from the finite-size scaling analysis of some of the low-energy excitations of the ES shown in Fig. 17.

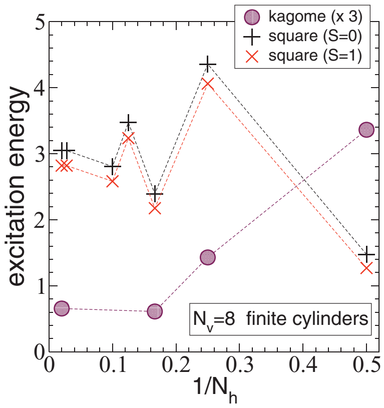

FIG. 17. (Color online) Finite-size scaling of the lowest-energy levels marked by arrows in the ES of Fig. 16. Excellent convergence is found when $N_h \to \infty$ (at constant $N_v = 8$). Note the alternating behavior according to the parity of $N_h/2$ for the square lattice, in contrast to the kagome lattice showing a straight exponential convergence.

APPENDIX B: FINITE-SIZE SCALING OF THE ENTANGLEMENT SPECTRUM VERSUS CYLINDER PERIMETER

After taking the limit of the infinite cylinder ($N_h \to \infty$), we investigate the dependence of the ES as a function of the cylinder perimeter N_v. Note that when taking the $N_h \to \infty$ limit, one still has to specify the choice of the B_L and B_R boundaries that uniquely determine the projector (even or odd) involved at the edges along the cut. Here, we only consider OBC, which select the integer spin sector of the boundary Hamiltonian. Our results are summarized in Fig. 18 for infinitely long cylinders with kagome and square lattices. A careful analysis of these spectra and of some of their low-energy excitations [see Fig. 19(a)] as a function of cylinder perimeter suggests that the square (kagome) lattice cylinder ES is gapped (gapless) in the limit $N_v \to \infty$. Since these features are opposite to what is expected in the corresponding bulk systems, we deduce that the ES characterizes specifically the nature of the edges [L and R in Figs. 1(a)–1(d)].

APPENDIX C: EXPANSION IN TERMS OF MANY-BODY OPERATORS

Any operator $\mathcal{O}_{\text{edge}}$ such as projectors $\mathcal{P}$ or boundary Hamiltonians acting on the edge can be expanded in terms of 3^{2N_v} orthogonal (real) operators $\hat{X}_\alpha$:

$$\mathcal{O}_{\text{edge}} = c_0 N_v + \sum_\alpha A_\alpha \, \hat{X}_\alpha \, . \tag{C1}$$

The scalar product in the operator basis is defined as $\langle \hat{u}\hat{v} \rangle$, where $\langle \ldots \rangle = \frac{1}{Z}\text{Tr}(\ldots)$ and the trace is *a priori* performed over the full basis of $Z = 3^{N_v}$ states. For convenience, the constant term $c_0 = \frac{1}{N_v}\langle \mathcal{O}_{\text{edge}} \rangle$ has been separated so that we can assume

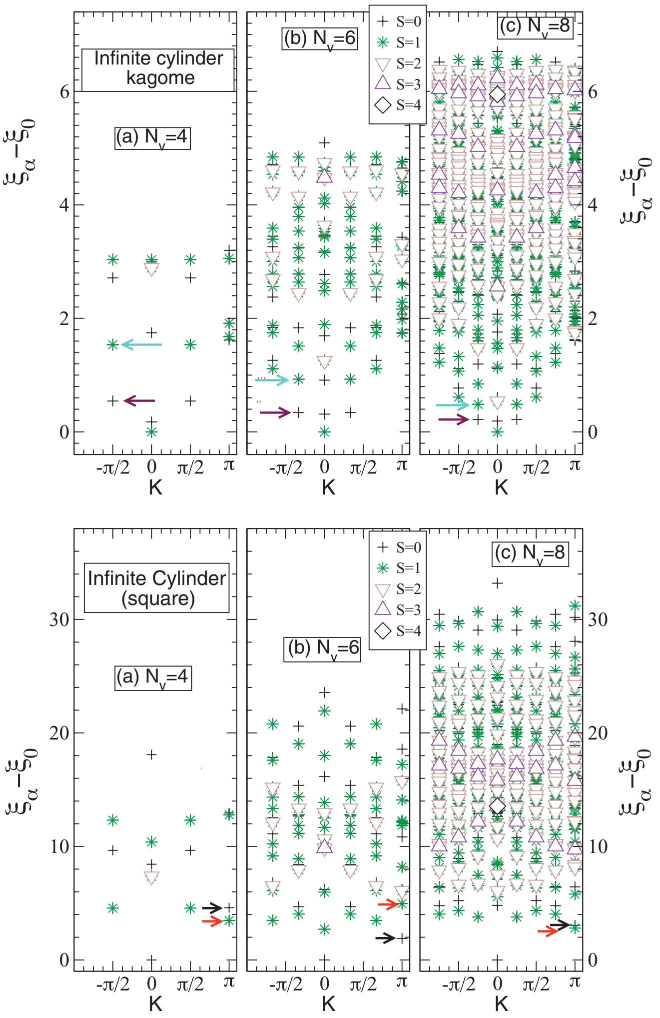

FIG. 18. (Color online) ES of infinite cylinders with increasing perimeter N_v. OBC are used for B_L and B_R. Kagome (top) and square (bottom) lattices.

all other operators satisfy Tr $\hat{X}_\alpha = 0$. Simple algebra shows that the coefficients can be obtained by taking the trace of the corresponding operators with $\mathcal{O}_{\text{edge}}$ as

$$A_\alpha = \langle \hat{X}_\alpha \mathcal{O}_{\text{edge}} \rangle / \langle \hat{X}_\alpha \hat{X}_\alpha^\dagger \rangle , \qquad \text{(C2)}$$

where the trace in the numerator involves, in fact, the sum over the projected subspace. We also obtain some "sum rule"

$$\langle \mathcal{O}_{\text{edge}}^2 \rangle = (c_0 N_v)^2 + \sum_\alpha A_\alpha^2 \langle \hat{X}_\alpha \hat{X}_\alpha^\dagger \rangle , \qquad \text{(C3)}$$

which enables us to compute the weight associated to each operator.

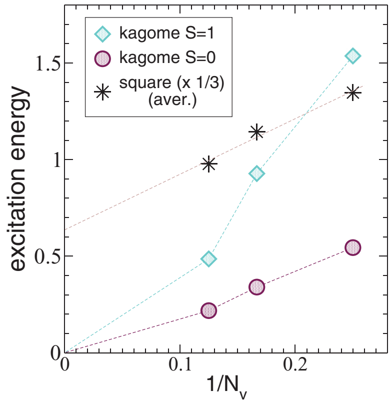

FIG. 19. (Color online) Finite-size scaling of low excitation energies of infinite cylinders vs inverse perimeter, suggesting a vanishing (finite) gap in the thermodynamic limit for the kagome (square) lattice. For the square lattice, the average (divided by 3) between the lowest $K = \pi$ singlet and triplet excitations is shown.

To go further and expand $\mathcal{O}_{\text{edge}}$ in the full operator basis, it is convenient to use a local basis of 9 (normalized) operators $\{\hat{x}_0, \ldots, \hat{x}_8\}$ which act on the local site configuration $\{|0\rangle, |1\rangle, |2\rangle\}$, e.g., $\hat{x}_0 = \mathbf{1}$, $\hat{x}_1 = \sqrt{\frac{3}{2}}(|0\rangle\langle 0| - |1\rangle\langle 1|)$, and $\hat{x}_2 = \frac{1}{\sqrt{2}}(|0\rangle\langle 0| + |1\rangle\langle 1| - 2|2\rangle\langle 2|)$, for the diagonal matrices, complemented by $\hat{x}_3 = \hat{x}_4^\dagger = \sqrt{3}|0\rangle\langle 1|$ acting as "spin" operators, and $\hat{x}_5 = \hat{x}_7^\dagger = \sqrt{3}|2\rangle\langle 0|$ and $\hat{x}_6 = \hat{x}_8^\dagger = \sqrt{3}|2\rangle\langle 1|$ acting as annihilation and creation (hard-core) bosonic operators. These operators satisfy $\text{tr}(\hat{x}_\lambda) = 0$ (for $\lambda \neq 0$) and $\text{tr}(\hat{x}_\lambda \hat{x}_\lambda^\dagger) = 3$, where "tr" is the trace over the local degrees of freedom (of some site i). From now on, we extend the action of these local operators to the whole edge, assuming a trivial (implicit) action on the $N_v - 1$ unspecified sites, i.e., $\hat{x}_\lambda^i \equiv \hat{x}_\lambda^i \otimes \mathbf{1}^{\otimes(N_v-1)}$, so that $\text{Tr}(\hat{x}_\lambda^i (\hat{x}_\lambda^i)^\dagger) = 3^{N_v}$ and $\langle \hat{x}_\lambda^i (\hat{x}_\lambda^i)^\dagger \rangle = 1$. Using the local basis of operators, one can then uniquely expand any edge operator like H_1 in terms of N-body operators as

$$\mathcal{O}_{\text{edge}} = c_0 N_v + \sum_\lambda c_\lambda \sum_i \hat{x}_\lambda^i + \sum_{\lambda,\mu,r} d_{\lambda\mu}(r) \sum_i{}' \hat{x}_\lambda^i \hat{x}_\mu^{i+r}$$
$$+ \sum_{\lambda,\mu,\nu,r,r'} e_{\lambda\mu\nu}(r,r') \sum_i{}' \hat{x}_\lambda^i \hat{x}_\mu^{i+r} \hat{x}_\nu^{i+r'} + \ldots , \qquad \text{(C4)}$$

where each group of terms involves products of $N = 1, 2, \ldots, N_v$ onsite operators $\hat{x}_\lambda^i$, i labeling the sites. Here, the sums do not contain the identity, and the sums over distances are restricted to nonequivalent relative distances. $\sum'$ means that only translations giving *distinct* sets of sites are performed (no multiple counting). Hence, the N-body *translationally invariant* operators $\hat{X}_\alpha$ in (C4), where α combines all the labels of the coefficients of the expansion [e.g., $\alpha = (\lambda, \mu, r)$ for $\hat{X}_\alpha = \sum_i' \hat{x}_\lambda^i \hat{x}_\mu^{i+r}$], are normalized as $\langle \hat{X}_\alpha \hat{X}_\alpha^\dagger \rangle = N_v / g_\alpha$, where g_α are "multiplicity" factors that count the number of times the operator maps onto itself under all N_v translations. The (real) coefficients in (C4) are obtained by taking the trace (in operator space) of the corresponding operators with the operator $\mathcal{O}_{\text{edge}}$:

$$c_\lambda = \frac{1}{N_v} \left\langle \left(\sum_{i=1}^{N_v} \hat{x}_\lambda^i \right) \mathcal{O}_{\text{edge}} \right\rangle , \qquad \text{(C5)}$$

$$d_{\lambda\mu}(r) = \frac{1}{N_v} \left\langle \left(\sum_{i=1}^{N_v} \hat{x}_\lambda^i \hat{x}_\mu^{i+r} \right) \mathcal{O}_{\text{edge}} \right\rangle , \qquad \text{(C6)}$$

$$e_{\lambda\mu\nu}(r,r') = \frac{1}{N_v} \left\langle \left(\sum_{i=1}^{N_v} \hat{x}_\lambda^i \hat{x}_\mu^{i+r} \hat{x}_\nu^{i+r'} \right) \mathcal{O}_{\text{edge}} \right\rangle , \qquad \text{(C7)}$$

where one can make advantage of translation symmetry to compute the right-hand side of these equations. The sum rule for the weights takes then the form

$$\frac{1}{N_v}\langle(\mathcal{O}_{\text{edge}})^2\rangle = c_0^2 N_v + \sum_{\lambda} c_\lambda^2 + \sum_{\lambda,\mu}\sum_{r}\frac{1}{g_r}d_{\lambda\mu}^2(r) + \sum_{\lambda,\mu,\nu}\sum_{r,r'}\frac{1}{g_{r,r'}}e_{\lambda\mu\nu}^2(r,r') + \dots, \quad \text{(C8)}$$

where the (second) sums are restricted to nonequivalent sets of distances and the multiplicity factors only depend on the latter.

---

[1] X. G. Wen, Int. J. Mod. Phys. B **5**, 1641 (1991).

[2] P. W. Anderson, Mater. Res. Bull. **8**, 153 (1973); P. Fazekas and P. W. Anderson, Philos. Mag. **30**, 432 (1974).

[3] A. Kitaev, Ann. Phys. (NY) **303**, 2 (2003).

[4] P. Mendels, F. Bert, M. A. de Vries, A. Olariu, A. Harrison, F. Duc, J. C. Trombe, J. Lord, A. Amato, and C. Baines, Phys. Rev. Lett. **98**, 077204 (2007), and references therein.

[5] G. Misguich and C. Lhuillier, in *Frustrated Spin Systems*, edited by H. T. Diep (World-Scientific, Singapore, 2005).

[6] Z. Y. Meng, T. C. Lang, S. Wessel, F. F. Assaad, and A. Muramatsu, Nature (London) **464**, 847 (2010); B. K. Clark, D. A. Abanin, and S. L. Sondhi, Phys. Rev. Lett. **107**, 087204 (2011).

[7] Y. Iqbal, F. Becca, and D. Poilblanc, New J. Phys. **14** (in press 2012).

[8] D. Poilblanc, M. Mambrini, and D. Schwandt, Phys. Rev. B **81**, 180402(R) (2010); D. Poilblanc and G. Misguich, *ibid.* **84**, 214401 (2011).

[9] Simeng Yan, David A. Huse, and Steven R. White, Science **332**, 1173 (2011).

[10] Hong-Chen Jiang, Hong Yao, and Leon Balents, arXiv:1112.2241.

[11] Hong-Chen Jiang, Zhenghan Wang, and Leon Balents, arXiv:1205.4289.

[12] S. Depenbrock, I. P. McCulloch, and U. Schollwöck, arXiv:1205.4858.

[13] A. Kitaev and J. Preskill, Phys. Rev. Lett. **96**, 110404 (2006); M. Levin and X.-G. Wen, *ibid.* **96**, 110405 (2006).

[14] H. Li and F. D. M. Haldane, Phys. Rev. Lett. **101**, 010504 (2008); R. Thomale, A. Sterdyniak, N. Regnault, and B. A. Bernevig, *ibid.* **104**, 180502 (2010); X.-L. Qi, H. Katsura, and A. W. W. Ludwig, *ibid.* **108**, 196402 (2012).

[15] D. Poilblanc, Phys. Rev. Lett. **105**, 077202 (2010); see also R. Thomale, D. P. Arovas, and B. A. Bernevig, *ibid.* **105**, 116805 (2010), using a "momentum cut."

[16] F. Verstraete and J. I. Cirac, arXiv:cond-mat/0407066; Phys. Rev. A **70**, 060302(R) (2004); J. I. Cirac and F. Verstraete, J. Phys. A: Math. Theor. **42**, 504004 (2009).

[17] J. I. Cirac, D. Poilblanc, N. Schuch, and F. Verstraete, Phys. Rev. B **83**, 245134 (2011).

[18] I. Affleck, T. Kennedy, E. H. Lieb, and H. Tasaki, Phys. Rev. Lett. **59**, 799 (1987); Commun. Math. Phys. **115**, 477 (1988).

[19] F. Verstraete, M. M. Wolf, D. Perez-Garcia, and J. I. Cirac, Phys. Rev. Lett. **96**, 220601 (2006).

[20] D. S. Rokhsar and S. A. Kivelson, Phys. Rev. Lett. **61**, 2376 (1988).

[21] R. Moessner and S. L. Sondhi, Phys. Rev. Lett. **86**, 1881 (2001); G. Misguich, D. Serban, and V. Pasquier, *ibid.* **89**, 137202 (2002).

[22] S. Furukawa and G. Misguich, Phys. Rev. B **75**, 214407 (2007); S. T. Flammia, A. Hamma, T. L. Hughes, and X.-G. Wen, Phys. Rev. Lett. **103**, 261601 (2009); J.-M. Stephan, S. Furukawa, G. Misguich, and V. Pasquier, Phys. Rev. B **80**, 184421 (2009); for Kitaev's toric code, see Hong Yao and Xiao-Liang Qi, Phys. Rev. Lett. **105**, 080501 (2010).

[23] J.-M. Stephan, G. Misguich, and V. Pasquier, J. Stat. Mech. (2012) P02003.

[24] Nevertheless, a dimer wave function on the kagome lattice can be mapped to Kitaev's toric code on the square lattice, which indicates that in the former case there should exist a nonlocal boundary Hamiltonian (Ref. 25).

[25] N. Schuch, D. Poilblanc, J. I. Cirac, and D. Pérez-García, arXiv:1203.4816.

[26] N. Schuch, I. Cirac, and D. Pérez-García, Ann. Phys. (NY) **325**, 2153 (2010).

[27] Hyejin Ju, A. B. Kallin, P. Fendley, M. B. Hastings, and R. G. Melko, Phys. Rev. B **85**, 165121 (2012).

[28] A. F. Albuquerque and F. Alet, Phys. Rev. B **82**, 180408 (2010).

[29] The critical or short-range behavior of the RVB wave functions can also be inferred from finite-size analysis of the correlation lengths obtained from the PEPS transfer matrices.

[30] Y. Zhang, T. Grover, and A. Vishwanath, Phys. Rev. B **84**, 075128 (2011).

[31] Fan Yang and Hong Yao, arXiv:1204.6381.

[32] N. Schuch *et al.* (unpublished).

[33] On the kagome lattice, H_{local} corresponding to the L and R edges differs slightly. Here, we refer to the L edge.

[34] D. Pérez-García *et al.*, New J. Phys. **12**, 025010 (2010).

[35] The trivial action of local operators on the unspecified sites is left implicit. Formally, $\hat{x}_\lambda := \hat{x}_\lambda \otimes \mathbf{1}^{\otimes(N_v-1)}$.

[36] M. Ogata, M. U. Luchini, S. Sorella, and F. F. Assaad, Phys. Rev. Lett. **66**, 2388 (1991).